LARGE-SCALE INVERSE MICROWAVE BACKSCATTER MODELING OF SEA ICE

Quinn P. Remund
Microwave Earth Remote Sensing Laboratory
Brigham Young University,
Provo, Utah

Abstract

Polar sea ice characteristic provide important inputs to models of several geophysical processes. Many forward electromagnetic scattering models have been proposed to predict the normalized radar cross section, σ^o, from sea ice characteristics. These models are based on very small-scale ice features and generally assume that the region of interest is spatially homogeneous. Unfortunately, spaceborne scatterometer footprints are very large (5-50 km) and usually contain very heterogeneous mixtures of sea ice surface parameters. In this paper, we apply scatterometer data to large scale inverse modeling. Given the limited resolution, we adopt a simple geometric optics forward scattering model to analyze surface and volume scattering contributions to observed Ku-band signatures. A model inversion technique based on recursive optimization of an objective function is developed. Simulations demonstrate the performance of the method in the presence of noise. The inverse model is implemented using Ku-band image reconstructed data collected by the NASA scatterometer. The results are used to analyze and interpret a σ^o phenomenon occurring in the Arctic.

Introduction

Several satellite instruments have proven the utility of scatterometers in monitoring the Arctic and Antarctic regions. Among these is the NASA scatterometer (NSCAT). Ku-band NSCAT data have been used in a number of cryosphere studies [1, 2]. NSCAT observations can be interpreted through accurate backscatter modeling. Forward scattering models have been developed to relate key surface parameters to these observed signatures. Many critical sea ice parameters are of interest to the field of cryosphere remote sensing [3]. Among these are thickness, surface roughness, salinity, snow cover, and age. An accurate knowledge of these parameters, among others, is important in understanding various geophysical processes such as local and global weather patterns, atmospheric and oceanic circulation, and heat transfer cycles. While directly estimating the parameters mentioned can be difficult, we propose a step in this direction through a better understanding of large-scale sea ice scattering properties. Rather than deal with small-scale ice characteristics, we adopt a simplified modeling approach to infer key electromagnetic scattering characteristics. These are, of course, related to the desired physical properties of the sea ice.

Thus, this paper describes the development and implementation of a large-scale model inversion methology based on a simple forward scattering model. The goal of the study is to provide an automated means for the inversion of microwave scattering models over vast regions rather than small individual homogeneous regions. The resulting sea ice parameter maps allow for interpretation of the evolution of scattering mechanisms over the entire cryosphere.

The NSCAT Instrument and Image Reconstruction

Microwave σ^o signatures of sea ice contain important information about surface characteristics. The goal of inverse modeling is to extract or estimate those parameters from σ^o measurements. The observed signatures are also a function of instrument design and measurement collection specifications such as frequency, polarization, spatial footprint size, and incidence angle. This section describes the NSCAT instrument used cand the image reconstruction algorithms used to produce the enhanced resolution imagery.

NSCAT has a number of characteristics that make it useful in monitoring sea ice [2]. It is a dual-polarization Ku-band scatterometer with multiple fan beams. Multiple NSCAT passes over the polar regions are used to reconstruct σ^o imagery. To improve the nominal resolution of NSCAT measurements, resolution enhancement algorithms can be applied to generate images. These methods rely upon a parameterization of the dependence of σ^o on incidence angles. Various order models can be used with increasing sensitivity to noise as order is increased. In general, σ^o (in dB) can be modeled with by

$$\sigma^\circ(dB) = A + B(\theta - 40^\circ) + C(\theta - 40^\circ)^2 + \ldots \quad (1)$$

where θ is the incidence angle, A is σ^o normalized to 40°, B is the linear incidence angle dependence of σ^o, C is the quadratic incidence angle dependence of σ^o, and so forth. For a limited range of incidence angles of [20°, 60°] NSCAT σ^o is found to have a nearly linear dependence on θ. Higher order models can be used to more accurately represent the dependence though the higher coefficients become increasingly sensitive to noise.

Several reconstruction methods exist for the generation of scatterometer imagery. For this study a polar stereo-

graphic projection was used in all image products. The AVE algorithm is one reconstruction technique for scatterometer image production [4]. A polynomial fit is used for each pixel to estimate the pertinent coefficients. For a particular pixel, the polynomial fit measurement set consists of all the measurements whose spatial footprint response include that pixel. AVE images are produced for each polynomial coefficient.

Another image reconstruction method is the scatterometer image reconstruction (SIR) algorithm [4]. SIR is a modified multivariate multiplicative algebraic reconstruction technique which uses multiple passes of a satellite instrument to increase spatial resolution. SIR results in increased reconstruction artifacts as well as increased resolution. For this reason, only the first order σ^o vs. θ model is used for SIR imagery.

Large-scale Forward Modeling of Sea Ice Backscatter

Forward models of sea ice backscatter have been developed which predict σ^o as a function of incidence angle and important surface parameters. Various sea ice characteristics affect observed signatures. For example, surface roughness reduces specular reflections and increases backscatter. Geophysically, this parameter is important in modulating wind sheering forces on the ice pack and can be an indicator of internal stresses. Liquid water content also influences backscatter signatures. Increased water content results in less penetration by incident microwave pulses. Hence, the backscatter is dominated by the surface scattering response. Snow cover adds another layer to the multilayer structure. Very dry snow appears electrically transparent at many microwave frequencies. However, as snow liquid water content increases, the sea ice signature is increasingly masked. In addition, sea ice salinity plays a role in determining backscatter responses. Brine pockets increase the effective permitivitty and provide volume scattering elements. Since brine pockets are commonly ellipsoidal in shape, the orientation of these inclusions influence the σ^o polarization response. Both snow cover and brine pocket distribution are closely related to sea ice age. Older ice forms typically have greater accumulated snow cover. Also, sea ice aging results in increased brine drainage. Volume scattering air bubbles often remain in the place of old brine inclusions.

A simple forward scattering model assumes that sea ice scattering consists of incoherently summed surface and volume scattering responses [5, 6],

$$\begin{aligned} \sigma^\circ_m &= \sigma^\circ_s + \sigma^\circ_v \\ \sigma^\circ_m &= \sigma^\circ_s + t^2\left(\frac{n\sigma_b}{2\alpha}\right)cos\theta_i \end{aligned} \tag{2}$$

where

σ°_m measured σ^o,
σ°_s surface scattering σ^o,
σ°_v volume scattering σ^o,
θ_i measurement incidence angle,
t plane wave power transmission coefficient,
n number density of scatterering elements,
σ_b σ^o per particle,
α volume attenuation coefficient.

This bulk model does not require a detailed description of the ice medium. Instead, several large scale parameters are used to represent the mean response in the region of interest. Following Swift [6] three primary volume scattering parameters are combined into one variable, the volume scatter albedo given by

$$\eta = \frac{n\sigma_b}{\alpha}. \tag{3}$$

Though it is a general parameter, η is related to sea ice features such as the number of volume scattering brine pockets and air bubbles. It is also sensitive to the effective permitivitty of the sea ice layers below the surface. Highly saline brine pockets have higher σ_b than air bubbles resulting in greater η values for the same number density, n.

Surface scattering is also an integral component of the backscatter model. Assuming that the surface can be modeled as an ensemble of reflective facets with Gaussian slope distributions, a geometric optics solution can be used [6, 7] so that,

$$\sigma^\circ_s = \frac{r(0)e^{-tan^2\theta_i/2S^2}}{2S^2cos^4\theta_i}, \tag{4}$$

where

$r(0) = 1 - t(0)$ nadir power reflection coefficient,
S RMS surface slope.

The geometric optics solution is derived under the assumption that the wavelength is significantly smaller than the typical roughness dimensions. At 14 GHz, the corresponding wavelength is approximately 2.1 cm. Hence, the model accounts for roughness features which are much larger than this, while smaller roughnesses may not be fully accounted for in the model. We expect that large surface roughness due to wave action and ice pack sheering forces are within the bounds of this assumption. However, very small-scale roughness due to such phenomena as wind roughening and small surface inhomogeneities are not accounted for in the model. For the purposes of this paper, we define $\beta = 2S^2$ to simplify the model inversion.

Figure 1 shows the total scattering v-pol responses for sample $r(0)$, β, and η values. The plots illustrate that the theoretical σ^o vs. θ signatures can not always be fit with a linear approximation between 20° and 60°. A

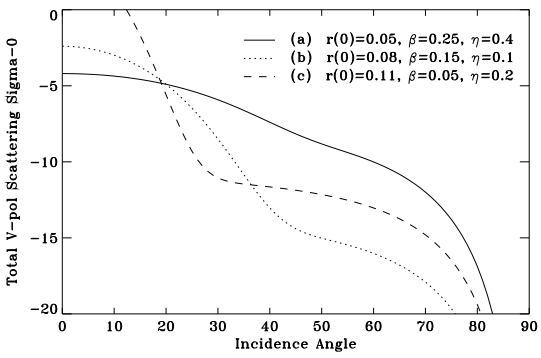

Figure 1: Model generated composite (volume + surface) v-pol scattering responses for sample combinations of $r(0)$, β, and η. The curves show the nonlinear nature of σ^o as a function of incidence angle.

linear model is appropriate for plot (a), but (b) and (c) clearly require higher order terms to accurately represent the incidence angle dependence. In general, the linear dependence assumption does not fit well in scenarios with relatively low β values. Swift was able to fit such plots to SASS σ^o observations of multiyear ice in the Arctic, demonstrating the ability to invert the model and estimate the three fundamental parameters.

Model Inversion Methodology

The theoretical scattering model proposed by Swift is defined by three basic parameters, $r(0)$, β, and η. These values can be estimated from observed NSCAT σ^o signatures given sufficient incidence angle sampling. In this section, an automated inversion technique is presented for determining the three parameters from NSCAT reconstructed imagery.

The inversion approach consists of the automated steepest descent optimization of an objective function. The objective function provides of measure of the error between observed signatures and estimated model parameters,

$$J(\sigma^\circ, r(0), \beta, \eta) = \sum_{\theta_i=40}^{60} [\sigma^\circ(\theta_i) - \sigma^\circ_m(\theta_i)]^2 \quad (5)$$

where

J	total squared modeling error,
$\sigma^\circ(\theta_i)$	observed σ^o at θ_i,
$\sigma^\circ_m(\theta_i)$	modeled σ^o at θ_i
$\vec{h}$	vector containing $[r(0), \beta, \eta]^T$.

Hence, $J(\sigma^\circ, \vec{h})$ is a measure of the accuracy of the model parameters in the prediction the observed signature. The $\sigma^\circ(\theta_i)$ response is computed given the σ^o vs. θ variable order polynomial fit coefficients for a particular pixel in the reconstructed imagery. Since total squared error is a sufficient statistic for mean squared error, the inversion method is a minimum mean squared error technique. Simulated three-dimensional objective functions (given an observed σ^o signature) indicate that the function has a well defined minimum within the range of expected $r(0)$, β, and η. Hence, the optimal parameters are found at the $\vec{h}$ yielding minimum $J(\sigma^\circ, \vec{h})$.

One method of automated optimization of an objective function is the steepest descent approach. Steepest descent locates the minimum of a function in an iterative fashion through the estimation of the local slope. The slope is obtained from the partial derivatives of the objective function. We define $G(\sigma^\circ, \vec{h})$ as a vector containing the negative partial derivatives. $G(\sigma^\circ, \vec{h})$ can be computed for any location vector $\vec{h}$ and points in the direction of steepest descent.

A recursive algorithm for computing the model parameters, and thus searching for the minimum of $J(\sigma^\circ, \vec{h})$ is given by,

$$\vec{h}(m+1) = \vec{h}(m) + \Delta(m) \odot G(m), \quad m =, 0, 1, 2, \ldots \quad (6)$$

where

Δ	vector of step sizes for each model parameter,
$\odot$	Schur element by element vector product.

The step size Δ can be chosen in a number of ways. Steepest descent algorithms often use step sizes that are a function of the objective function. Hence, smaller steps are taken closer to the minimum. For this study, a fixed step size is used,

$$\Delta = [0.001,\ 0.002,\ 0.002]^T \quad (7)$$

yielding model parameter estimate resolutions of 0.001, 0.002, and 0.002 for $r(0)$, β, and η, respectively.

The algorithm is initialized with arbitrary $\vec{h}(0)$. Simulations indicate that the minimum is found as long as $\vec{h}(0)$ is in the range of possible sea ice parameter values. For a given image set of polynomial fit coefficients, the algorithm is run for each pixel. The resulting products are images of $r(0)$, β, and η used in determining the spatial distribution of important surface parameters.

The algorithm has various strengths that make it useful in model inversion. First, the proposed algorithm is fully automated. Many previous inverse modeling studies focusing on fitting observed and forward modeled signatures have relied on user interface to manually perturb the model parameters until a satisfactory match is obtained. The technique presented in this paper requires no user interaction and quickly estimates model parameters given an observed σ^o vs. θ response. This facilitates the production of model parameter image sequences from scatterometer imagery. In addition, if the the σ^o incidence

angle dependence model is sufficient (of high enough order) the algorithm finds the best parameters in the minimum mean squared error sense.

The estimated parameters provide, in effect, the mean responses over the pixel region. These are useful on a macroscopic level when viewing entire sea ice packs. We note that the products of the inversion technique have limited utility on very small scales; because the model is based on a specific forward model, the quality of the resulting parameter estimates are directly related to the quality of the original forward model. We expect some error since the forward model does not account for such things as complex sea ice permitivitties and small-scale roughness features.

Inverse Model Simulations

To evaluate the capability of the inversion technique, simulations are designed and implemented. First, the "ground truth" model parameters $r(0)$, β, and η are run through the forward model to produce a σ^o vs. θ response. This signature is then sampled in incidence angle between 20° and 40° to simulate scatterometer measurement collection. At this point, Monte Carlo scatterometer noise is added to each measurement using the noise model,

$$\sigma_n^\circ(\theta_i) = \sigma^\circ(\theta_i)(1 + N(0, k_p)) \tag{8}$$

where

$\sigma_n^\circ(\theta_i)$ noise-added σ^o at incidence angle θ_i,
$\sigma^\circ(\theta_i)$ original noiseless σ^o,
$N(0, k_p)$ normally distributed random variable.

The multiple noise-corrupted measurements are used to obtain polynomial fit coefficients. Variable degree polynomials are used to determine the effect of model order on the inversion. The coefficients are then input to the inverse model resulting in surface parameter estimates. Error analysis is performed with the original parameter values and the inverse model results.

For 6 day NSCAT images generated at the SIR and AVE spatial resolutions of 4.45 km, average pixel regions usually encounter at least 10 hits. Hence, for the simulations, incidence angle sampling is performed randomly from a uniform distribution between 20° and 60° with 10 samples for each realization. In addition, measurement noise is simulated using Eq. 8 and various k_p values. Typical NSCAT k_p levels are in the range 0 to 0.1. In fact, for the NSCAT Antarctic v-pol data collected from 1996 day 270 to 275, 97% of the k_p values are below 0.1 and 86% are below 0.05.

To offer near-comprehensive simulations which consider a broad range of ($r(0)$, β, η) triplet combinations, synthetic "ground truth" images are constructed of each parameter that represent all possible sample combinations of the parameters within the ranges,

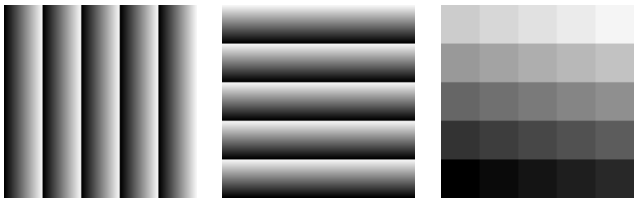

(a) $r(0)$ (b) β (c) η

Figure 2: "Truth" parameter images, $r(0)$, β, and η, used in the model simulations.

$$r(0)\epsilon[0.01, 0.3],$$
$$\beta\epsilon[0.05, 0.4],$$
$$\eta\epsilon[0.05, 0.4].$$

These values represent ranges which cover typical sea ice surface parameters. The images are generated using 25 evenly spaced samples of each parameter resulting in 25^3 combinations. Figure 2 shows the truth images. These are input to the simulation process through the generation of noise-corrupted polynomial coefficient images which used as inputs to the inverse model.

The simulations are run using the 10 incidence angle sample scheme described previously. Noise levels (k_p) are considered at 0.02 increments from 0 to 0.1. The results are summarized graphically in Figures 3-5. In Figure 3, the $r(0)$ estimates are shown with k_p values of 0, 0.04, and 0.08. The image frames demonstrate increasing ability in the algorithm to accurately represent the left-to-right increasing gradient as model order increases. Nearly all images show that the algorithm has difficulty in areas corresponding with very low β values. As previously noted, extremely low β correspond to scattering responses that are primarily contained below the 20° limit for NSCAT data. The images also exhibit that higher order models are increasingly sensitive to noise evident as speckling in the estimate frames. Thus, a trade off exists between ability to estimate parameters accurately (on average) and sensitivity to measurement noise.

The performance of the algorithm in estimating β is shown in Figure 4. The image panels reveal that first-order coefficients are not sufficient to accurately represent surface roughness induced characteristics of the forward scattering model. The first-order frames are nearly constant in value. In contrast, the second to fourth-order models are much more successful in reproducing the upward β gradients in the truth image. Like $r(0)$, the β estimates are increasingly sensitive to noise as order increases.

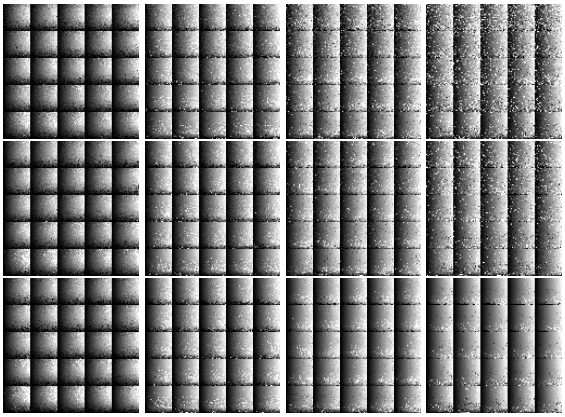

Figure 3: Inverse model $r(0)$ parameter estimates at various σ^o vs. θ model orders and noise levels. Columns contain increasing model orders. Rows contain increasing k_p from 0 to .08 at .04 increments.

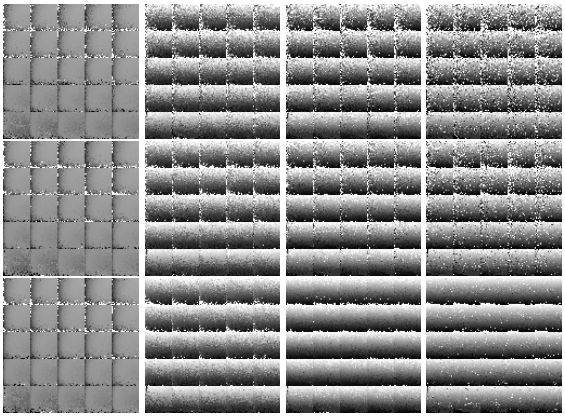

Figure 4: Inverse model β parameter estimates at various σ^o vs. θ model orders and noise levels. Columns contain increasing model orders. Rows contain increasing k_p from 0 to .08 at .04 increments.

Estimates of the final parameter, η are shown in Figure 5. Similar trends with order value exist for η estimates as with the previous two. The first-order model has difficulty generating the constant frames in the truth image. However, all of the higher order models appear to perform relatively well.

In order to provide a quantitative measure of algorithm performance over all the possible parameter combinations, the median absolute error is used. This metric is computed for each parameter as the median of the ensemble of absolute errors over the entire truth image. The estimate images have few very large errors caused by poor sampling or extreme noise. However, the few outliers can skew an average error metric. The median absolute error is used to reduce the confusing effects of theses outliers.

In the interest of space, the corresponding error plots are not included. However, all of the plots indicate that parameter estimate error is lower for higher order models in the absence of noise. However, as k_p rises, the second or third-order estimates have the lowest median absolute error. The curves also show that higher order models are increasingly sensitive to k_p evident in steeper slopes in the error plots. The first-order model is relatively insensitive to k_p in all three figures since this model performs the most averaging. From these results, we conclude that the second or third order σ^o vs. θ polynomial coefficients provide the best inputs to the inverse model in the presence of noise. Since both offer similar error characteristics, the second order model will be used in the implementations with actual NSCAT data presented in the following section.

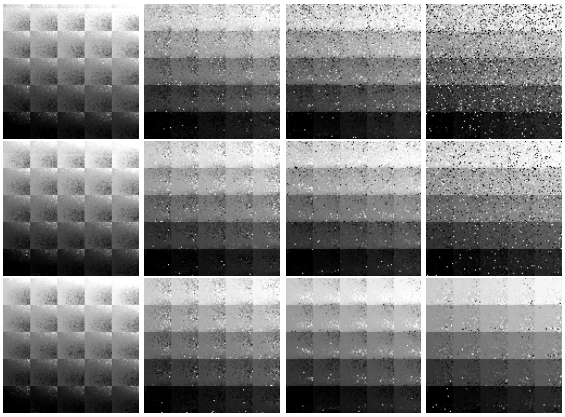

Figure 5: Inverse model η parameter estimates at various σ^o vs. θ model orders and noise levels. Columns contain increasing model orders. Rows contain increasing k_p from 0 to .08 at .04 increments.

Results

The inversion method is applied to second-order NSCAT reconstructed v-pol AVE imagery (A_v, B_v, and C_v) to study the behavior of the technique and to interpret phenomenon observed in the reconstruction σ^o images. A set of three Arctic AVE images representing the onset of Arctic summer is used as inverse model inputs. The ice masked image series is illustrated in Figure 6. The Arctic ice pack is characterized by large regions of multiyear ice exhibiting high A_v values near the centers of the images. Younger forms of ice have lower A_v signatures. The phenomenon examined in this sequence is the annual drop in σ^o observations due to the passage of warm fronts over the ice pack inducing significant surface melting. While the first images have high multiyear σ^o signatures differentiating this ice type from lower σ^o first year ice, by the end of the image sequence, the two types are indistiguishable.

Figure 7 contains the image estimates of Arctic $r(0)$. We note that the noisy values near the pole are due to insufficient incidence angle sampling caused by satellite orbit geometry and the NSCAT measurement collection

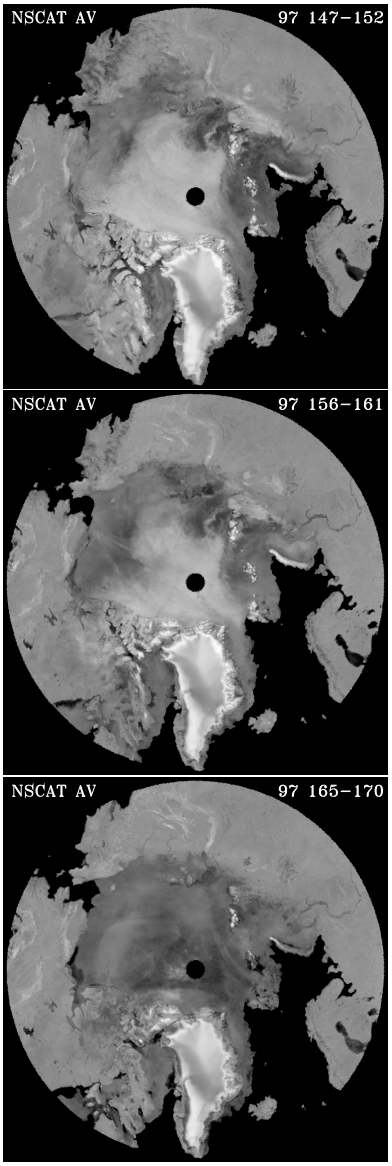

Figure 6: Ice masked NSCAT Arctic A_v SIR image series.

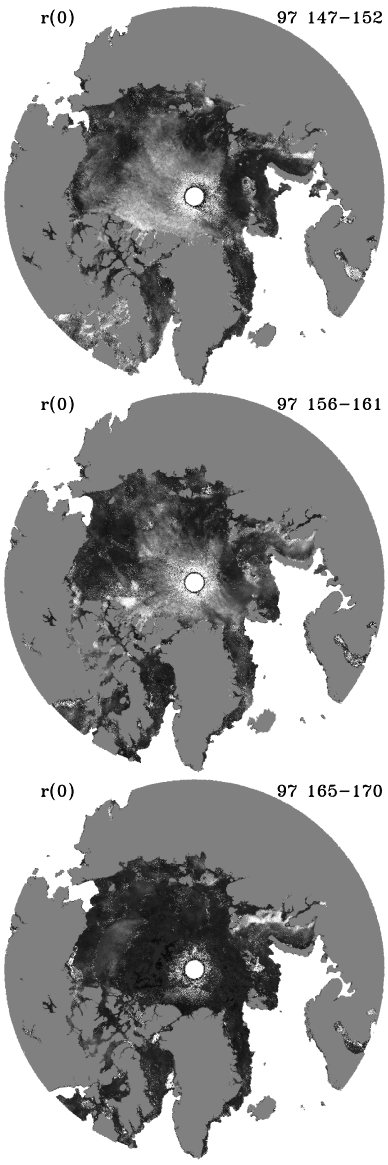

Figure 7: Inverse model estimates of Arctic $r(0)$. The greyscale image display range is $r(0)\epsilon$[0,0.1].

configuration. Unsatisfactory sampling of the incidence angle spectrum results in poor estimates of polynomial fit coefficients in the image reconstruction. Consequently, very low confidence is placed on the near-pole parameter estimates. The general trend in the $r(0)$ imagery consists of relatively high and low values for multiyear and first year sea ice, respectively. The melt event causes $r(0)$ to drop quickly over the entire multiyear area.

The spatial distribution of β surface roughness values are shown in Figure 8. Multiyear ice has typically high β levels in contrast to lower observations over first year ice. Newer ice forms are typically less deformed than old ice that has been subjected to wave deformation, ice pack sheering, and large-scale roughness caused by melt and freeze cycles. As the sequence progresses, β values drop until nearly the entire multiyear region appears similar to the first year β observations. The source of the change may be due to surface smoothing of features due to melting and the creation of melt ponds.

The final estimate images of Arctic volume scattering albedo is shown in Figure 9. These images illustrate the intense volume scattering contributions characteristic of multiyear ice. Varying levels of η within multiyear regions can be related to the number density of volume

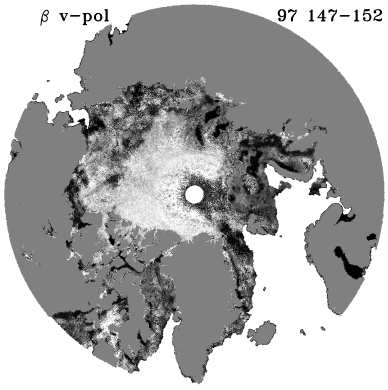

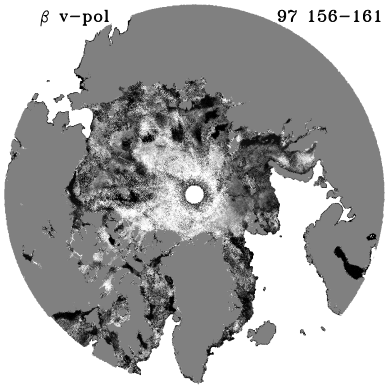

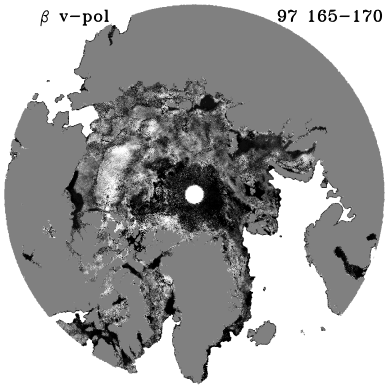

Figure 8: Inverse model estimates of Arctic β. The greyscale image display range is $\beta\epsilon$[0.1,0.45].

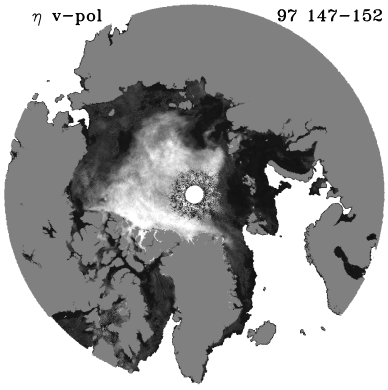

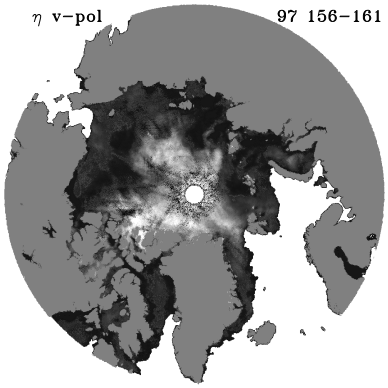

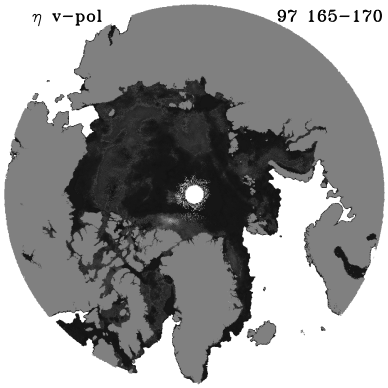

Figure 9: Inverse model estimates of Arctic η. The greyscale image display range is $\eta\epsilon$[0,0.45].

scatterers and mean volume scattering element cross sections. Areas of younger ice have much lower η due to higher salinity and dielectric loss. The image progression shows η decreasing as temperature rises and surface melting occurs. In the last image frame, volume scattering has been almost completely masked by increased water content which reduces penetration depth. Such signature masking makes the various ice types competely indistiguishable at Ku-band.

These results illustrate the utility of the inverse model in interpretting the sources of scattering phenomena observed in the reconstructed NSCAT imagery. Since the method is fully automated, large ensembles of measurements can be inverted providing estimates of the spatial distribution and magnitude of important surface parameters. These parameters can then be related to sea ice types as previously described. In general, older ice types such as multiyear ice exhibit very high $r(0)$ and η values in the absence of significant surface melt. In contrast, first year ice and other relatively young ice types have much lower $r(0)$ and η. Smoother ice types have typically lower β levels. Temporal variations in the parameters can be used to understand the evolution of scattering

mechanisms within the various ice types as considered in this section.

Conclusions

This study has presented an inversion technique applied to a simple, but robust forward scattering model. The method is fully automated requiring no user interface. Consequently, large scatterometer polynomial fit coefficient images representing the incidence angle dependence of σ^o can be used as inputs to the inverse model. The algorithm is used to determine the spatial distribution of three important surface parameters, the power reflection coefficient at nadir, $r(0)$, the RMS surface slope, S (represented by $\beta = 2S^2$ in the inverse model), and the volume scattering albedo, η.

Simulations of the method demonstrate the capability of the algorithm. Higher order incidence angle dependence models yield better estimates of the surface parameters in the absence of noise. When noise is introduced, a trade-off exists between the capability to estimate a wide range of possible parameter combinations and sensitivity to noise. The first order model performs reasonably well for $r(0)$ and η estimation but cannot effectively reproduce true β values. A good balance is found in using a second order model.

The inverse model is applied to NSCAT Arctic image sequences. The results show that the parameter images have consistent spatial distributions. The method is also used to analyze drastic σ^o decreases over multiyear ice in the Arctic as the summer season begins. The accompanying surface melt causes all three parameters to decrease abruptly. Surface roughness appears to be reduced and increased water content masks the volume scattering contribution that give multiyear ice its characteristically high σ^o signature.

References

[1] Q.P. Remund and D. Long, "Sea-Ice Extent Mapping Using Ku-Band Scatterometer Data," *J. of Geophys. Res*, vol. 104, no. C4, pp. 11515-11527, 1999.

[2] D.G. Long and M.R. Drinkwater, "Cryosphere Applications of NSCAT Data," *IEEE Trans. on Geosci. and Rem. Sens.*, vol. 37, no. 3, pp. 1671–1684, 1999.

[3] F. Carsey, "Review and status of remote sensing of sea ice," *IEEE Journal of Oceanic Engineering,* vo. 14, pp. 127-137, 1989.

[4] D. Long, P. Hardin, and P. Whiting, "Resolution Enhancement of Spaceborne Scatterometer Data," *IEEE Trans. on Geosci. and Rem. Sens.*, vol. 31, pp. 700–715, 1993.

[5] F.T. Ulaby, R.K. Moore, and A.K. Fung, *Microwave Remote Sensing – Active and Passive*, Vol. 3, Norwood, MA: Artech House Inc., 1985.

[6] C.T. Swift, "Seasat Scatterometer Observations of Sea Ice," *IEEE Trans. on Geosci. and Rem. Sens.*, vol. 37, no. 2, pp. 716-723, Mar. 1999.

[7] D.E. Barrick, "Rough Surfaces," in *Radar Cross-Section Handbook*, G.T. Ruck, Ed. New York: Plenum, 1970, pp. 671-772.